SYNTHESIS AND CHARACTERIZATION OF SOLID STATE

ELECTROLYTE FOR SODIUM-ION BATTERIES

A DISSERTATION

SUBBMITTED IN PARTIAL FULFILMENT OF THE

REQUIREMENTS FOR THE AWARD OF THE DEGREE

OF

MASTERS OF SCIENCE IN PHYSICS

Submitted by:

PUNEET KUMAR (2K22/MSCPHY/32)

SOURAV MEENA (2K22/MSCPHY/41)

Under the supervision of

DR. AMRISH K. PANWAR

(ASSISTANT PROFESSOR)

DEPARTMENT OF APPLIED PHYSICS

DELHI TECHNOLOGICAL UNIVERSITY

(Formerly Delhi College of Engineering)

Bawana Road, Delhi-110042

JUNE, 2024

CANDIDATE'S DECLARATION

We, **PUNEET KUMAR**, Roll No. **2K22/MSCPHY/32** and **SOURAV MEENA**, Roll No. **2K22/MSCPHY/41** hereby certify that the work which is presented in the thesis entitled "**SYNTHESIS AND CHARACTERIZATION OF SOLID STATE ELECTROLYTE FOR SODIUM-ION BATTERIES**" in partial fulfilment of the requirement for the award of the Degree of Master of Science in Physics submitted in the Department of Applied Physics, Delhi Technological University, Delhi is an authentic record of our own work carried out during the period from August 2023 to June 2024 under the supervision of **Dr. Amrish K. Panwar**.

The matter presented in the thesis has not been submitted by me for the award of any other degree of this or any other institute. The work has been accepted in a peer reviewed Scopus indexed conference with the following details:

Title of the Paper: Impact of Calcination Temperature on Structural Properties of $Na_3Zr_2Si_2PO_{12}$ as a Solid Electrolyte for Na-ion Batteries

Author names: Sourav Meena, Puneet Kumar, Naveen, Sharad Singh Jadaun and Dr. Amrish K. Panwar

Name of Conference: International Conference on Atomic, Molecular, Material, Nano and Optical Physics with Applications (ICAMNOP–2023).

Dates with the venue: 20th-22th December, 2023, Delhi Technological University, Delhi – 110042 (India).

Conference Registered: Yes.

Status of paper (Accepted/Published/Communicated): Accepted.

Date of paper communication: 11th April, 2024.

Date of paper acceptance: 5th June, 2024.

Place: Delhi   **Puneet Kumar**   **Sourav Meena**
Date: June 7, 2024   (2K22/MSCPHY/32)   (2K22/MSCPHY/41)

This is to certify that the students have incorporated all corrections suggested by the examiner in the thesis and examiner in the thesis and the statement made by the candidate is correct to the best of our knowledge.

Signature of Supervisor

i

DEPARTMENT OF APPLIED PHYSICS

DELHI TECHNOLOGICAL UNIVERSITY

(Formerly Delhi College of Engineering)

Bawana Road, Delhi-110042

CERTIFICATE

I, hereby certify that the Project Dissertation titled **"SYNTHESIS AND CHARACTERIZATION OF SOLID STATE ELECTROLYTE FOR SODIUM-ION BATTERIES"** which is submitted by **PUNEET KUMAR**, Roll **No. 2K22/MSCPHY/32** and **SOURAV MEENA**, Roll **No. 2K22/MSCPHY/41,** Department of Applied Physics, Delhi Technological University, Delhi in partial fulfilment of the requirement for the award of the degree of Master of Science, is a record of the project work carried out by the students under my supervision. To the best of my knowledge this work has not been submitted in part or full for any Degree or Diploma to this University or elsewhere.

Place: Delhi

Date: 07/06/2024

Dr. Amrish K. Panwar

Assistant Professor
Department of Applied Physics
Delhi Technological University
(Formerly Delhi College of Engineering)
Bawana Road, Delhi - 110042

<u>ACKNOWLEDGEMENT</u>

TABLE OF CONTENTS

ABSTRACT

Rechargeable batteries have the potential to revolutionize sustainable energy storage, with applications in small portable devices and electric vehicles. The solid-state sodium-ion battery is expected as substitute to present commercial lithium-ion battery due to its rich sodium supplies, low cost, and high safety standards. Conventional electrolytes are often made up of an organic solvent and salts with strong conductivity, that ensures close contact with the electrodes and makes battery construction easier. Solid-state electrolytes are a crucial component of sodium-ion batteries require strong ionic conductivity while being operationally safe and simple to construct. In this study, $Na_3Zr_2Si_2PO_{12}$ (NZSP) electrolyte has been synthesised through solid-state route at different temperatures. X-ray diffraction characterization has been performed to confirm phase of NZSP. Strain and average crystallite size of NZSP has been calculated by Williamson-Hall plot using XRD peaks. Morphological examination has been done by scanning electron microscope (SEM) which revealed agglomeration and nonuniformity of particles. Pellet of bare NZSP electrolyte has been sintered, and its impedance spectroscopy characterization has performed in frequency range of 4 Hz - 8 MHz to evaluate ionic conductivity and dielectric properties. Furthermore, NZSP has been blended with polyethylene oxide (PEO) polymer to make composite electrolyte and its dielectric properties and ionic conductivity are studied.

LIST OF FIGURES

Figure 1.1: The electric battery tests conducted by Volta.

Figure 1.2: Discharging and charging of battery.

Figure 2.1: NASICON-type (a) rhombohedral structure and (b) monoclinic structure.

Figure 3.1: Schematic representation of preparation of NZSP1050 electrolyte pellet.

Figure 3.2: Stepwise preparation of NZSP1050-PEO composite electrolyte film.

Figure 3.3: Geometric conditions for diffraction from lattice planes.

Figure 3.4: Backscattered and Secondary electrons in SEM.

Figure 4.1: XRD patteren of NZSP calcinated at different temperatures.

Figure 4.2: W-H plot of NZSP calcinated at 1050 °C.

Figure 4.3: SEM images of NZSP1050 calcinated at 1050° C at the magnification of (a) 10,000 X and (b) 50,000 X.

Figure 4.4: FTIR pattern of NZSP calcinated at 1050 °C temperature.

Figure 4.5: Nyquist plot of sintered NZSP1050 pellet.

Figure 4.6: Nyquist plot of sintered NZSP1050-PEO film.

Figure 4.7(a): Dielectric constant versus log(freq.) of NZSP1050 pellet at various temperatures.

Figure 4.7(b): Dielectric constant versus log(freq.) of NZSP1050-PEO at various temperatures.

Figure 4.8(a): Dielectric loss versus log(freq.) of NZSP1050 pellet at various temperatures.

Figure 4.8(b): Dielectric constant versus log(freq.) of NZSP1050-PEO at various temperatures.

ABBREVIATIONS

Na-ion	Sodium-ion
Li-ion	Lithium-ion
P	Phosphorus
Na	Sodium
XRD	X-ray diffraction
SEM	Scanning electron microscope
PEO	Polyethylene oxide
NZSP	Sodium Zirconium Silicon Phosphate
FTIR	Fourier Transform Infrared Spectroscopy
SE	Secondary Electron
BSE	Backscattered Electron
PP	Polypropylene
PE	Polyethylene
SPE	Solid Polymer Electrolyte
NASICON	Sodium super Ionic Conductor

1

INTRODUCTION AND LITERATURE REVIEW

1.1 INTRODUCTION

In recent times, there has been a notable surge in the utilization of finite fossil fuels, raising concerns about the effects this has had on the environment. The significant emergence of new technologies has captured the attention of researchers. Renewable energy sources like solar, tidal, and wind power can reduce dependency on fossil fuels, but they are unreliable and require large storage costs [1, 2]. Advancements in energy storage and conversion technologies are crucial for everyday use. Energy storage is crucial in supplying uninterrupted electricity at a steady frequency to all electrical equipment. The market for sustainable energy sources like solar and wind is expanding quickly each year. Electric vehicles will eventually rule the road as a result of the global transportation sector becoming more electrified in an effort to combat global warming. However, renewable energy and vehicle electrification rely heavily on energy storage facilities. The construction of large-scale power storage facilities allows for a quick transition from non-renewable to renewable energy sources. Batteries are the first choice to store energy. In order to store and release energy, a battery undergoes an electrochemical redox reaction to transform chemical energy into electrical energy.

1.2 HISTORY OF BATTERIES

Alessandro Volta created the "electric pistol" as the first practical application of static electricity. He considered enabling long-distance communication, although just one Boolean bit. A wooden pole-supported iron wire intended to be extended from Como to Milan, Italy. The line would terminate in a jar that held methane gas. An electrical

spark would be transmitted through wire to explode the jar in order to signal a coded event. When some fluids were used as conductors, Volta discovered in 1800 that they could create a constant flow of electricity. This idea led to development of the first voltaic cell, or battery, as it is more often known. Further investigation showed to Volta that stacking voltaic cells on top of one another would increase voltage.[3]

Figure 1.1 The electric battery tests conducted by Volta.

William Cruickshank created the first electric battery that could be produced in large quantities in 1802. He assembled equal-sized square copper and zinc sheets into a long, rectangular wooden box, soldering them together. The metal plates were secured in place by grooves in the box. The electrolyte, or diluted acid, was then placed inside the sealed box. This was similar to the flooded battery that we still have in our possession.[3]

English scientist John F. Daniell created a better battery in 1836 that produced more consistent current than previous attempts to store electrical energy. Lead-acid based rechargeable battery technology was invented by Gaston Planté in 1859 and is still in use today. All batteries were primary up to that point, which meant they couldn't be reused.[4]

The nickel-cadmium (Ni-Cd) battery was created in 1899 by Swedish inventor Waldmar Jungner. Nickel served as positive electrode (cathode), while cadmium served as negative electrode (anode). After switching from cadmium to iron two years later, Thomas Edison named this battery nickel-iron (Ni-Fe). A low specific energy, poor low-temperature performance, and excessive self-discharge hampered the nickel-iron battery's success.

The majority of current research efforts are focused on enhancing lithium-based systems, which were initially brought to market by Sony in 1991. Li-ion batteries are utilised for electric cars and satellites in addition to powering computers, digital cameras, medical equipment, power tools, and mobile phones. Among the many

advantages of the battery are its high specific energy, ease of charging, low maintenance requirements, and environmental friendliness[5].

1.3 Components of Battery

The key parts of a battery are separator, electrolyte, cathode, and anode. A battery needs each and every one of its components to function; without one, the battery cannot operate.

1. **Cathode**

Through an electrochemical reaction, the oxidizing or positive electrode recognized as cathode absorbs electrons from external circuit and undergoes reduction. In general, the cathode dictates the battery's chemistry. which comes in a number of forms (for example, sodium metal oxide, alkaline, etc.).

2. **Anode**

Through an electrochemical process, the reducing or negative electrode, recognized as anode, undergo oxidation and releases electrons into the external circuit. Metals and other conductive materials are frequently used to create anodes.

3. **Electrolyte**

The electrolyte permits ions to move between the anode and the cathode. This media might be solid, liquid, or even gel. Electrolytes transport the ions necessary for electrochemical processes, and the kind of electrolyte varies depending on the cathode. Lithium-ion batteries, for example, often employ a liquid or gel electrolyte (such as lithium-polymer batteries).

4. **Separator**

Separators are porous materials that prevent direct contact between the anode and cathode, which might result in disastrous results such as the battery catching fire or even exploding. The separator allows ions to move. Separator works as a physical barrier to separate the anode and cathode. It avoids direct electron movement by

allowing only ions to pass through the tiny hole inside. Synthetic resins such as polyethylene and polypropylene are now commercially available separators.

1.4 Types of Battery

Batteries are categorised as -

(1) Primary

(2) Secondary

1.4.1 Primary battery

Primary/non-rechargeable batteries are pre-charged and ready to use, hold their charge for years when not used, and are designed for specific uses, so they do not require maintenance. Primary batteries may only be used once and must be replaced after being completely discharged. Furthermore, battery disposal is an environmental concern since the metals and compounds in these batteries can harm the environment if not disposed of appropriately. Some examples of primary batteries are - alkaline battery, zinc-carbon battery, etc.

1.4.2 Secondary battery

When current is passed in the opposite direction of discharge, a secondary cell or battery can be recharged to its pre-discharge condition. These are also called rechargeable batteries. Even after they have been fully depleted, secondary batteries may be recharged and used again. Secondary batteries must be carefully selected for their intended use, they are better for the environment, less expensive, and often deliver more power than disposable batteries. The most commonly used rechargeable battery types are lead acid, NiCd, NiMH, and Li-ion.

1.5 Working principle of battery

Anode (negative electrode), cathode (positive electrode), and electrolyte are the three main parts of a rechargeable battery or cell, as shown in Figure. A substance's or metal's affinity for electrons varies depending on its nature. When two distinct types of metals and their compounds are brought together by an electrolyte, an electrochemical potential form between them. Because the anode has a larger affinity

for electrons and becomes negatively charged [6] and the cathode is positively charged due to it's lower affinity for electrons. Positive ions flow through an electrolyte from anode to cathode due to electrochemical potential. The primary function of electrolytes is to inhibit electron conduction while allowing ion transport through them. When an ion travels from anode to cathode, the neutral charge distribution is perturbed; consequently, electrons begin to move via the external circuit to restore it. To prevent the battery from dying in absence of an external circuit, a capacitive charge builds up quickly. In the electrolyte region between the cathode and anode, a separator is inserted to prevent the battery from shorting out.
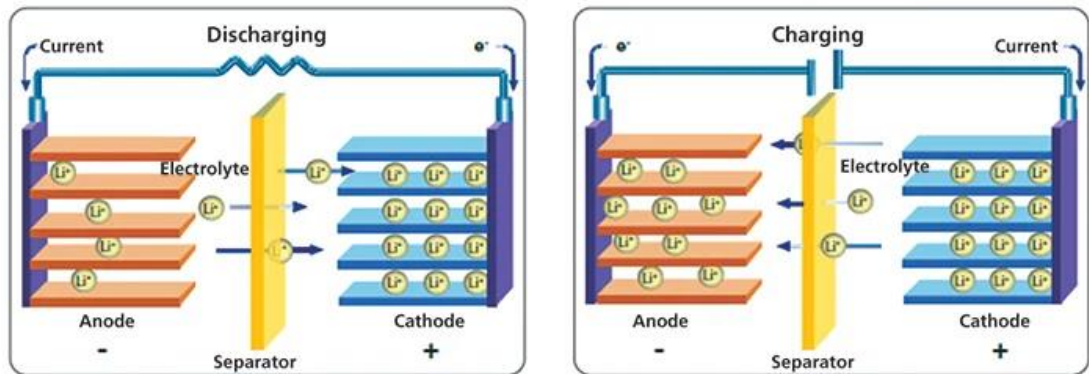
Figure 1.2 Discharging and Charging of battery[7].

2

ELECTROLYTES

2.1 Types of Electrolytes

1. Liquid Electrolyte

In most modern battery systems, solid electrodes and liquid electrolytes are the two main components. Among the many advantages of this configuration is that the liquid's presence reduces problems arising from volume variations, which are typically the consequence of the electrode materials' changing composition during charging and discharging. Other advantages include the fact that liquids' ionic conductivity is typically much higher than that of solids. An essential consideration is the range of potentials across which electrolytes are stable.[8]

2. Solid Electrolyte

Inorganic ceramics main material utilised as solid electrolytes in sodium-ion batteries. Solid electrolytes have a symmetrical skeletal structure and mobile ions. Mobile ions can travel across skeleton sites via point defects, resulting in ion conduction. Inorganic solid electrolyte's ionic conductivity depends on accessible hopping sites, energy barrier for hopping [9] and amount of mobile ions.

3. Polymer Electrolyte

Polymer electrolytes have benefits over ceramics due to their excellent ability to be processed and flexibility, while still retaining the benefits of solid electrolytes, such as stability in size and safety. the capacity to inhibit the growth of dendrites. Salts are present in certain polymer electrolytes. Some polymer chains are surrounded by solvent molecules, while in other cases a solvent is included to create a gel with polymer chains. In general, they are more mechanically robust, allowing for the creation of a standalone film and possess greater conductivities.[10]

4. Solid Polymer Electrolyte

The first SPE studied was a dry solid polymer electrolyte based on PEO. This system does not need organic liquid and is solvent-free. The ceramic-polymer composite electrolyte is created by combining active ceramics with polymer hosts. Composite electrolyte combines the benefits of organic polymer electrolytes and inorganic ceramic resulting in better ionic conductivity, mechanical properties, and chemical/thermal stability. In addition to serving as ionic conductors, SPEs are also used extensively in a variety of portable electronic devices, including thin credit cards, laptop computers and mobile phones. This eliminates the need for inert porous spacers in cells or batteries by acting as a separator between the electrolyte and electrode.[11]

2.2 ELECTROLYTE FOR SOLID-STATE SODIUM-ION BATTERY

Sodium is the most desirable substitute of lithium in terms of cost and environmental accessibility. Its abundance in the earth's crust is roughly 23,000 ppm compared to 20 ppm of lithium. Due to natural abundance of sodium resources and large capacity of metallic sodium anodes, rechargeable sodium-based batteries can be a more affordable alternative to lithium-ion batteries.[12] Traditional SIBs with flammable organic liquid electrolytes have a low energy density and associated safety issues like low thermal stability and quick flammability. Research is being done on sodium-ion batteries, the next generation of batteries, which use solid electrolytes instead of liquid ones in order to improve battery safety and dependability. It is believed that the two main barriers for development of solid-state batteries are high interfacial resistance between solid electrolytes and electrode materials and lower ionic conductivity of solid electrolytes. Solid electrolytes have the dual benefits of being non-flammable and having the ability to prevent Na-dendrite development while a battery is in operation. Na-ion serves as the mobile ion in these rechargeable batteries. Na-ions travel via the electrolyte and electrolyte-electrode interfaces from negative electrode (anode) to positive electrode (cathode) during discharging, while electrons start to flow from cathode to anode through an external circuit to maintain neutral charge distribution. The motions of electrons and ions are inverted during charging[13]. Although the essential functioning mechanism of both batteries are same. Electrolyte in solid-state sodium-ion batteries is unlike from that in conventional batteries, in

that it acts as a separator as well as an electrolyte. As a result, electrolytes play a crucial role in rechargeable sodium-ion battery systems.

For the effective execution in sodium batteries, electrolytes must full-fill several preconditions, including –

1. Environmental and Economic Viability
2. Non-flammable
3. High Ionic Conductivity
4. Wide Electrochemical Stability Window
5. Thermal Stability
6. Compatibility with Electrode Materials
7. Chemical Stability
8. Low Toxicity

2.3 SODIUM ZIRCONIUM SILICON PHOSPHATE ($Na_3Zr_2Si_2PO_{12}$) A SOLID ELECTROLYTE

NASICON (Na Super Ion Conductor) is a potential oxide-based electrolyte with 3D tunnels for Na ion movement. In 1976, Goodenough and Hong synthesized and characterized the first NASICON compound, Na_{1+x} $Zr_2Si_xP_{3-x}O_{12}$ ($0 \leq x \leq 3$). This compound has since gained popularity as a solid-state electrolyte for sodium-ion batteries. NASICONs have high stability under air and moisture, large electrochemical windows, and ionic conductivity of roughly 10^{-3} S cm^{-1} at ambient temperature, making them suitable as next-generation batteries [14]. In the Na_{1+x} $Zr_2Si_xP_{3-x}O_{12}$ ($0 \leq x \leq 3$) system compositions displayed the characteristic rhombohedral structure having space group R3c with space group number 167, whereas certain compositions with $1.8 \leq x \leq 2.2$ exhibited monoclinic structure of space group C2/c and space group number 15. Below 423 K, a phase transition to the monoclinic structure induced by shear deformation would occur. Nevertheless, solely the rhombohedral phase demonstrated superionic conductivity due to its increased symmetry. Figure 2.1 (a) represents the NASICON-type rhombohedral structure of NZSP and Figure 2.2 (b) represents the NASICON-type monoclinic structure of NZSP.

NASICONs' ionic conductivity was impacted by a number of variables, including synthetic techniques and chemical composition, in addition to their crystal structure. An illustration of this is seen with $Na_{3.4}Zr_2Si_{2.4}P_{0.6}O_{12}$, which displayed a notable ionic conductivity of $\sim 10^{-3}$ S/cm at ambient temp. when x = 2.4, achieved through a solution-assisted solid-state reaction. Researchers Roy and Kumar observed a significant impact on the ionic conductivity of $Na_3Zr_2Si_2PO_{12}$ based on the arrangement of Si/P as revealed by molecular dynamics simulation. In the rhombohedral structure with six basal planes, enhancing Na^+ conductivity was possible by having one phosphorous and two silicon atoms due to the lower energy barriers resulting from the stronger coulombic repulsion of Na^+/P^{5+} compared to Na^+/Si^{4+}. Moreover, the volatilization of sodium post-calcination at high temperatures necessitated the addition of excess Na_2CO_3, Na_2O, or other sodium compounds to maintain the stoichiometric ratio in $Na_3Zr_2Si_2PO_{12}$. The introduction of excess Na is found to widen bottleneck size of conducting channel, boosting grain conductivity. Small additional amounts of sodium are advantageous in reducing the crystallization temperature of NASICON and minimizing the emergence of ZrO_2.
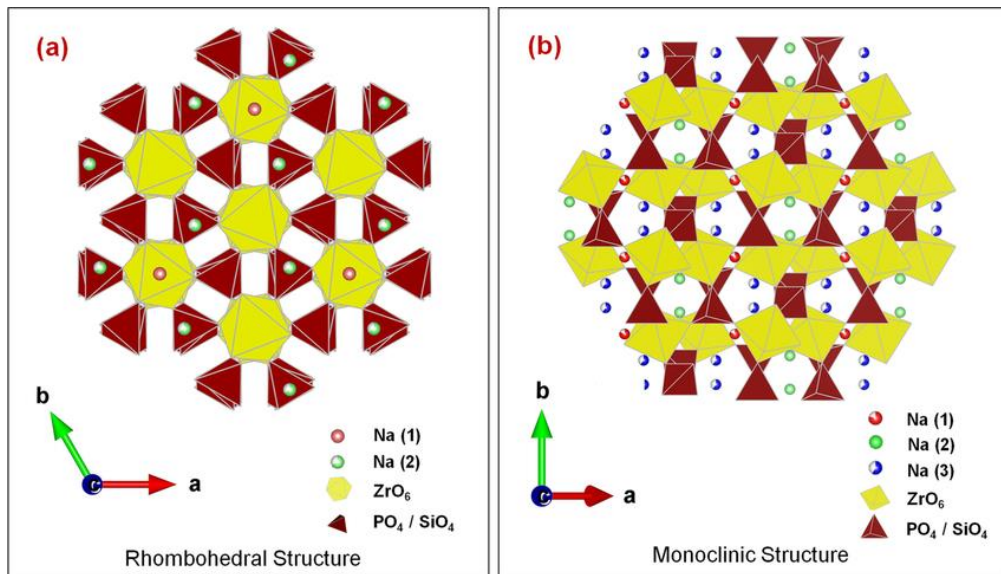

Figure 2.1 NASICON-type (a) rhombohedral structure and (b) monoclinic structure [15].

The NASICON sintered around 1100°C accomplished conductivity of $\sim 1.13 \times 10^{-3}$ S/cm. However, escalating the calcined temperature from above 1100 °C led to a decline in ionic conductivity due to increased volatilization at the higher temperature.

2.4 CHALLANGES

1. Interfacial Resistance

One of the most significant concerns is the high interfacial resistance between the NZSP electrolyte and the sodium metal anode. This high resistance might restrict the movement of ions, lowering the battery's overall performance. Techniques such as adding a thin gold interlayer have been explored to reduce this resistance or by employing polymer interlayer between electrolyte and electrode can also reduce resistance [16].

2. Mechanical Stability and Dendrite Formation

Dendrite production is owing to the flaws, fractures, and cavities that are already present inside solid electrolyte. Since sodium dendrites have the potential to form and pierce the electrolyte, resulting in short circuits and a shorter battery life, the mechanical stability of NZSP is essential. Composite electrolytes incorporating materials like epoxy have been developed to improve mechanical stability and inhibit dendrite growth [17]. NZSP-Polymer hybrid electrolyte is capable to enhance mechanical stability and supress dendrite formation. Therefore, it will be highly desired to create electrolytes that combine the benefits of both solid ceramic and polymer electrolytes.

3. Low Ionic Conductivity

NZSP typically exhibits lower ionic conductivity at room temperature, which limits the efficiency of sodium-ion transport within the battery. Efforts to enhance conductivity include doping with fluorine (F^-), which has shown to increase the conductivity significantly [18]. Ionic conductivity of NZSP can be enhanced by sintering proper temperature or by doping of other elements.

2.5 OBJECTIVES OF RESEARCH WORK

The main goal of this research is to synthesize and characterize to examine structural, morphological, electrical, and dielectric characteristics of the solid electrolyte NZSP and NZSP-PEO composite.

3

SYNTHESIS AND CHARACTERIZATION

3.1 SOLID STATE REACTION

This method uses solid reactants for producing polycrystalline materials. Typically, reaction begins at a very high temperature. Chemical and morphological features of reactants, including free energy, surface area, and reactivity, changes with solid-state route, and also with other reaction circumstances like reaction environment, temperature, and pressure, all have an impact on solid-state reactions. The advantages of the solid-state reaction process are its simplicity and bulk manufacturing.

Solid-state reactions are sluggish due to the inhomogeneity of the reactants at the atomic level, even if they are well mixed at the particle level (1 µm or 10 mm scale). To generate the proper ratio of desired element atomic-level mixing of reactants is done by solid-state counter diffusion of ions to bring atoms together of the various elements [19].

3.2 MATERIAL SYNTHESIS

Solid-state route has been used to synthesis of NZSP. All the precursors Na_2CO_3 (99%, Sigma Alderich), SiO_2 (99%, Sigma Alderich), ZrO_2 (99%, Sigma Alderich) and $NH_4H_2PO_4$ (98%, Sigma Alderich) were taken in stoichiometric ratio. 10 % excess sodium and phosphorus precursors were taken, because of their volatility at high temperatures [20]. All Precursors were hand grinded using agate mortar pestle. Isopropanol (IPA) was used for wet grinding medium to get homogeneous mixture of sample. After Grinding sample was calcinated at different temperatures (950 °C-1150 °C) using alumina crucible in muffle furnace for 10 hours. The sample of NZSP calcined at 1150 °C, 1050 °C and 950 °C are abbreviated as NZSP1150, NZSP1050 and NZSP950 respectively. The calcinated samples were then ground into fine powder. After phase formation, NZSP1050 was grinded with polyvinylpyrrolidone (PVP)

binder for pellet preparation. NZSP1050 pellet was prepared using a pelletizer. Pellet was sintered at 1150 °C using a muffle furnace. After sintering, aluminium metal electrodes were coated on both sides of pellet using thermal vapour deposition technique. Figure 3.1 shows the schematic representation of preparation of NZSP1050 pellet.
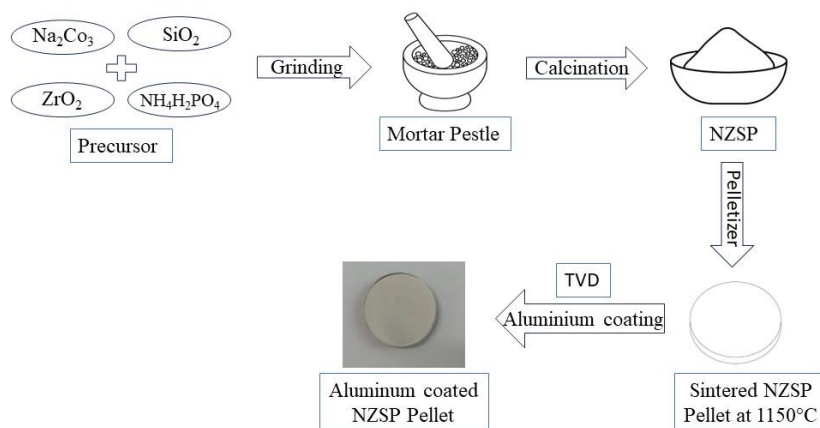

Figure 3.1 Schematic representation of preparation of NZSP1050 pellet.

NZSP1050-PEO composite electrolyte film was also prepared. NZSP1050 was sonicated in dimethylformamide (DMF) solvent using a sonicator to produce consistent size fine particles of NZSP1050. The composite film was formed by combining NZSP1050 crystallites with PEO (MW 300000 g/mol) polymer in a 1:10 stoichiometric weight ratio with DMF as a solvent. The mixture was agitated with a magnetic stirrer at 50˚C for 18 hours, resulting in a uniformly viscous slurry. Slurry was placed in a Petri dish and vacuum dried at 55˚C for to eliminate any remaining solvent. Figure 3.2 shows the schematic representation of preparation of NZSP1050-PEO composite electrolyte film.
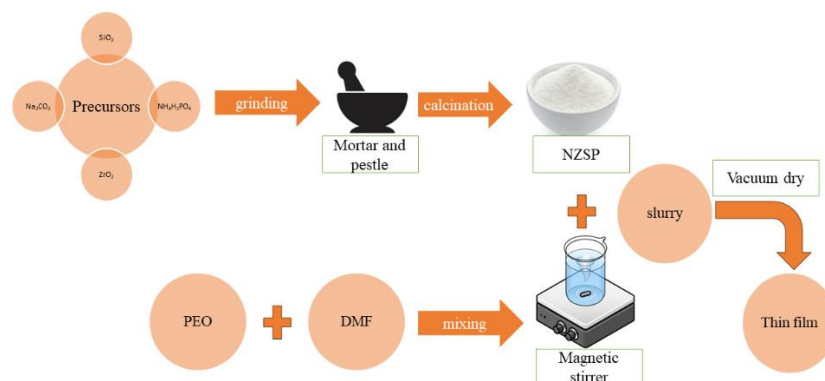
Figure 3.2 Stepwise preparation of NZSP1050-PEO composite electrolyte film.

3.3 MATERIAL CHARACTERIZATION

XRD pattern of NZSP950, NZSP1050, and NZSP1150 were measured by employing Bruker D-8 X-Ray Diffractometer with Cu-Kα radiations at 1.540 Å. XRD intensity data was collected across a 2θ range of 12˚ to 50˚, with 0.01 increments. The observed XRD data was refined using the X'Pert High-Score software. The morphological examination of NZSP is carried out by an FEI Nova NanoSEM 450 scanning electron microscope. PerkinElmer Fourier transform infrared spectroscopy spectrum II was used to record FTIR data in range of 3000-500 cm^{-1}. Impedance spectroscopy was also performed on the NZSP1050 pellet of diameter 13mm in the frequency range of 4Hz to 8 MHz and NZSP-PEO film which has a diameter of roughly 19 mm, across the frequency range of 4Hz to 4 MHz using an HIOKI make 3536 LCR oscilloscope.

3.4 X-RAY DIFFRACTION (XRD)

Crystal materials can be recognized and described using X-ray diffraction (XRD), a conventional technique. An X-ray pattern unique to each crystalline solid serves as a "fingerprint" for identification. The approach is based on the sample's X-ray diffraction in multiple directions. There is significant diffractive interference with waves at wavelengths close to the crystal lattice spacing. With a wavelength of 1.54 Å, copper is utilized as source of X-ray. The measurement of diffracted X-ray intensity is based

14

on the diffraction angle (2θ). The atomic structure can be inferred from the peak's intensity. The crystal's perfection is reflected in the peak's sharpness and form.
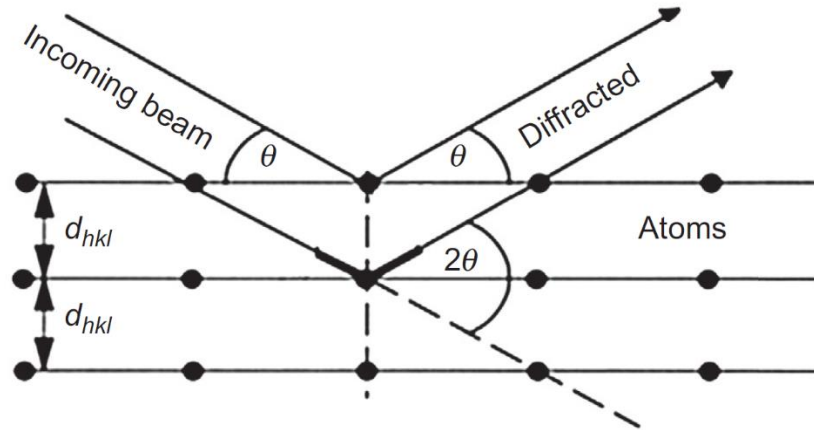

Figure 3.3 Geometric conditions for diffraction from lattice planes.

The intensity Vs 2θ plot-

(i)   provides structural information about the material. The presence or absence of specific sets of peaks corresponding to distinct planes determines the crystal formations.

(ii)   The movement of peaks from their initial locations in bulk crystals indicates stresses in the material.

W.L. Bragg provided a geometrical description of the XRD phenomena, known as constructive interferences. The figure 3.3 illustrates geometrical conditions of diffraction and deduction of Bragg's law. Bragg's law is provided as an Equation (3.1).

$$2dsin\theta = n\lambda \tag{3.1}$$

In Equation (3.1), n represent order of diffraction, θ is angle of diffracted beam, λ is x-ray wavelength and d is the interplanar spacing. Diffraction follows Bragg's equation for constructive interference when it happens along each lattice plane and direction in a polycrystalline, untextured material containing small grains.

For qualitative analysis, X-ray diffraction is primarily used, despite being a quantitative process. Any crystalline solid, including organic materials, metals, insulators, polymers, ceramics, and thin film powders, is subject to this kind of analysis. For both single crystals and powders, X-ray diffractometers can be employed. While single crystal diffractometers are used to research molecular structure, powder diffractometers are used to analyse phases, however the latter may also be used to extract molecular information. [21]

3.5 SCANNING ELECTRON MICROSCOPY (SEM)

SEM is a strong and efficient imaging tool. A vacuum system and lenses are used to generate an electron beam, and the surface is scanned at magnifications range of 1 µm - 1 nm, it depends on the hardware used. Elemental analysis at the specimen surface is investigated using an energy-dispersive spectrometer and SEM. Backscattered electrons and secondary electrons are two new features of SEM imaging that have greatly expanded scanning potential. The electron gun, together with other components, form the heart of SEM.[22]

Figure 3.4 depicts the employment of both secondary (SE) and backscattered electrons (BSE) to generate a better resolution picture. By convention, emitted electrons with an energy of less than 50 eV are classified as secondary electrons. SEs are formed by the inelastic collision of the specimen's electrons with incoming electron beam. The term SE describes the electrons that are expels from the valence shell. Electrons released with energy greater than 50 eV are referred to as backscattered electrons. BSE are electrons of beam that scatter back from specimen. Possibility of emitting BSE electrons increases as the atomic number increases. The picture brightness and BSE signal both rise as the atomic number increases[23].
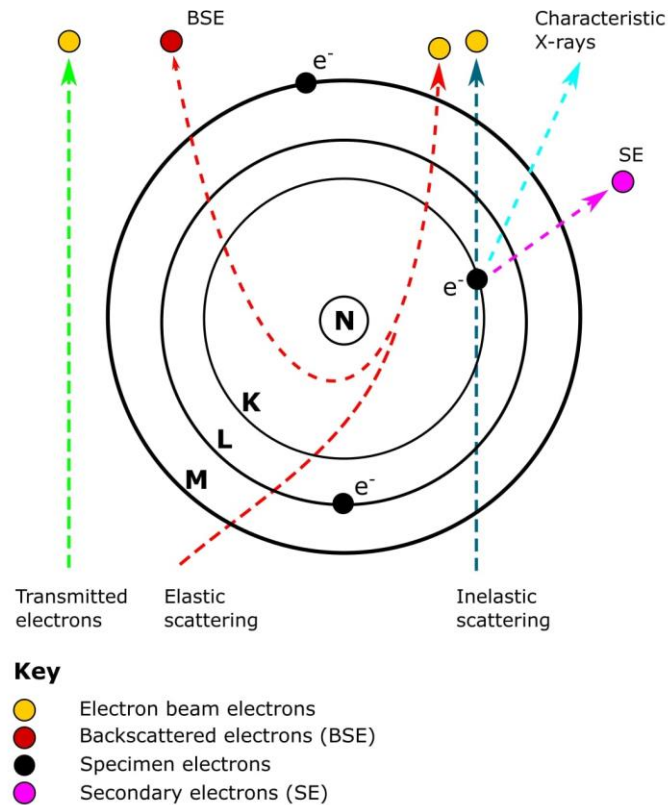
Figure 3.4 Backscattered and Secondary electrons in SEM

3.6 FOURIER TRANSFORM INFRARED (FTIR) SPECTROSCOPY

One quick, low cost, easy to use, and non-destructive characterization is FTIR spectroscopy. Although FTIR is a very useful characterization for recognition of pure compounds, its applicability to chemical mixtures is limited. The methodology is predicated on the identification of functional groups within molecules that undergo vibrations (either through stretching or bending) in response to specific light wavelengths. The FTIR spectrum is generated by graphing the intensity of vibrations (% transmission) versus the light frequency (cm^{-1}) to which the sample is exposed. The fingerprint region pertains to specific sections of the FTIR spectrum that are distinct to the substance under examination.[24].

3.7 IMPEDANCE SPECTROSCOPY (IS)

Cells with two identical electrodes are frequently attached to the surfaces of a sample in cylindrical or parallelepiped order to study the electrochemical behaviour of electrode and electrolyte materials. Vacuum or neutral atmosphere (e.g. argon) are all commonly used. To conduct an experiment, apply a known voltage or current to the electrodes and measure reaction. Impedance spectroscopy aims to identify the time-invariant properties of electrode-material systems and their relationships with controllable variables like temperature and static voltage or current bias.

When a cell is electrically stimulated, a variety of fundamental microscopic processes occur throughout the cell, which, when combined, result in the overall electrical response. Electrons are transported through electronic conductors, transferred at Through oxidation or reduction reactions, charged or uncharged atomic species from cell materials or the atmosphere interact with the electrode-electrolyte interface and pass through electrolyte defects. The electrodes' and electrolyte's ohmic resistance as well as the reaction rates at the electrode-electrolyte interface control the flow rate of charged particles, or current. Band structural anomalies at grain boundaries, especially in the presence of second phases, and point defects in materials can hinder flow. [25] Impedance (Z) is comparable to resistance: it measures a circuit's capacity to resist current. Resistance is a notion for ideal resistors; however, many circuits are more complicated hence impedance is used to substitute resistance. Along with inductance, resistance, and capacitance, impedance takes into account every property that makes up an ideal resistor. Because impedance is a complex number, it may be shown as a Nyquist plot. The shape of the semicircle on this plot typically represents a charge transfer process, and its size indicates the quantity of charge transfer resistance that is present. On the other hand, this plot (also referred to as the Warburg impedance) might show up as a straight line with a positive slope if the process involves diffusion. This figure is also circuit-dependent (parallel, series, or combinations). Besides from Nyquist plots, impedance may also be represented as a Bode plot [26].

4

RESULTS AND DISCUSSION

4.1 XRD ANALYSIS

The XRD patterns for NZSP calcinated at different temperatures (1150°C, 1050°C, and 950°C) is shown in figure 4.1. The patterns reveal that the sample calcinated at 950°C does not demonstrate complete NZSP phase development, but the sample calcinated at 1050°C shows proper NZSP phase formation when compared to the JCPDS file (84-1200). It was discovered that raising the temperature to 1150°C caused a minor movement in the peak locations. At 1050°C, NZSP exhibits a monoclinic phase of space group c2/c with space group no. 15. The lattice parameters a, b, and c are 1.5651 nm, 0.9055 nm, and 0.9220 nm, respectively, with β = 123.742° (angle between b and c). Slight ZrO_2 impurity might have existed due to the low reactivity of the monoclinic ZrO_2 utilized as the precursor, or because volatile elements such as P and Na were lost in high-temperature synthesis [20, 27]. It is worth noting that when more Na is given to NZSP, impurities such as Na_3PO_4 are often detected, but this time they are not evident in the NZSP1050. It means that Na_3PO_4 is either equally distributed across the NZSP matrix or dispersed into the parent phase [28].
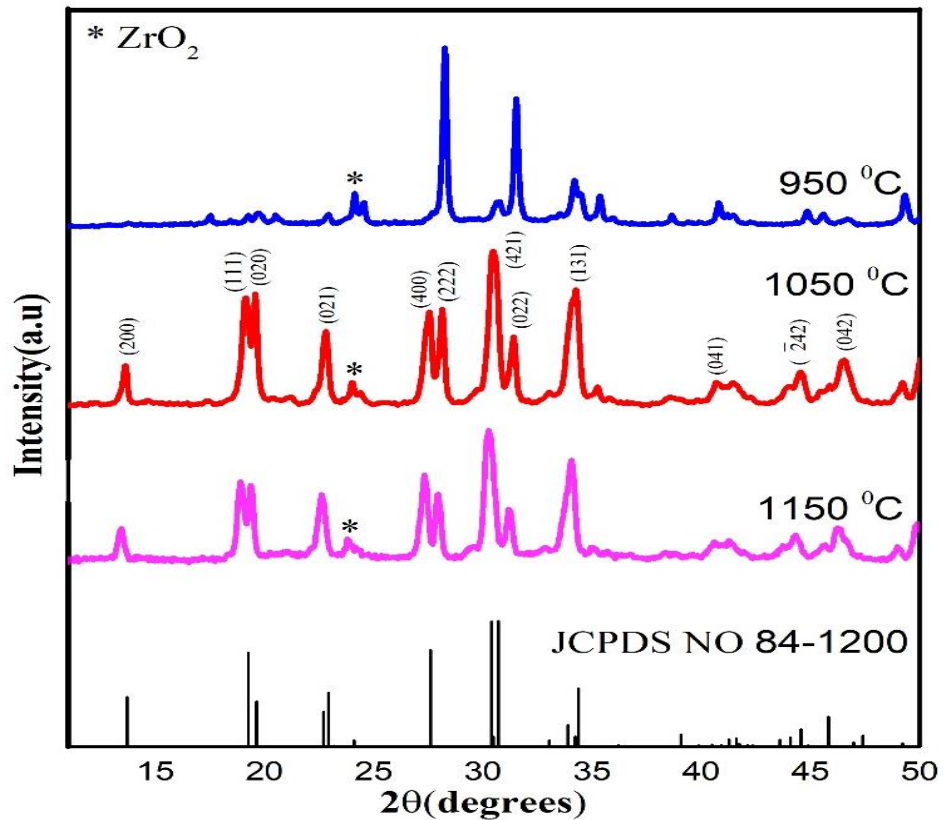
Figure 4.1 XRD patteren of NZSP calcinated at different temperatures.

In Figures 4.2, the microstrain value and crystallite size is calculated using Williamson-Hall plot from Equation (4.1).

$$\beta \cos\theta = \frac{K\lambda}{D} + 4\,\varepsilon \sin\theta \qquad (4.1)$$

Slope and intercept of linearly fitted graph between $4\sin\theta$ and $\beta\cos\theta$ represent microstrain and crystallite size, respectively. The plot for NZSP shows a crystallite size of 133 nm and a microstrain of 2.43×10^{-3}.
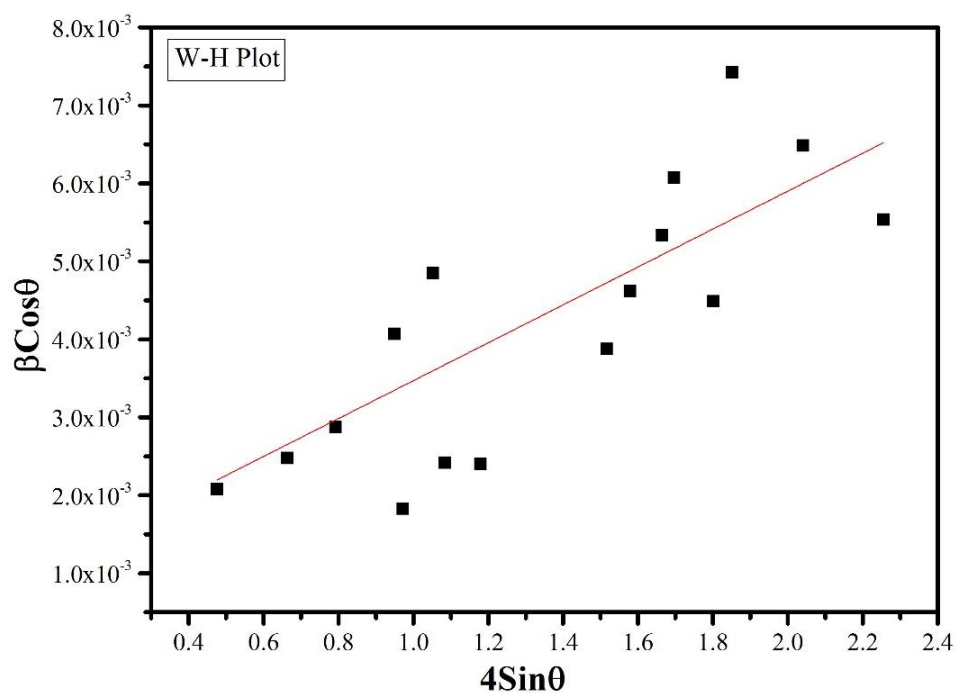
Figure 4.2 W-H plot of NZSP calcinated at 1050 °C.

4.2 MORPHOLOGICAL ANALYSIS

Figure 4.3 shows SEM images of the synthesized NZSP1050 sample prior to integration into the host matrix. Figure 4.3 (a) shows low magnification pictures of NZSP1050 powder with agglomerated, nonuniform, and dispersed particle morphology, which might be attributable to the lack of a sintering process. Figure 4.3 (b) shows sample characteristics at greater magnification, confirming strong agglomeration and nonuniform spherical morphology with average particle sizes ranging from 0.32 μm to 0.52 μm.
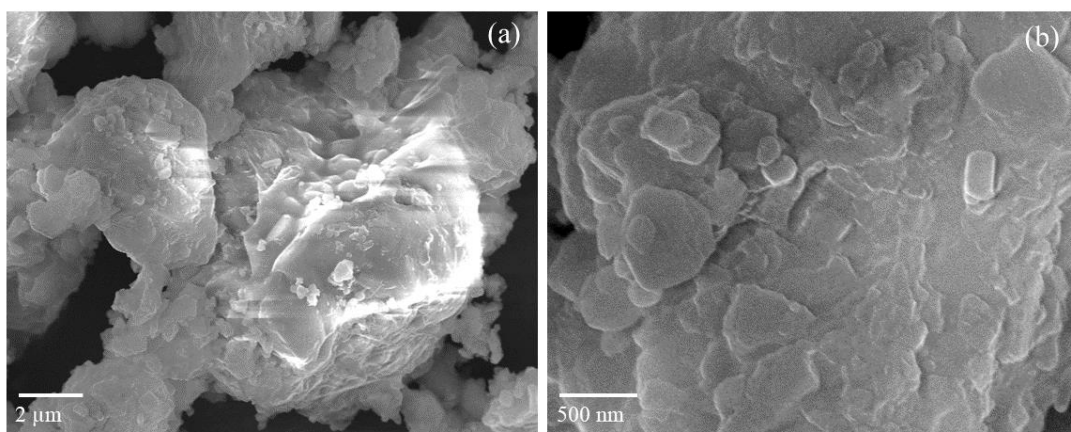
21

Figure 4.3 SEM images of NZSP1050 calcinated at 1050° C at the magnification of (a) 10,000 X and (b) 50,000 X

4.3 FTIR ANALYSIS

FTIR measurements were performed to indicate the existence of several functional groups in NZSP1050 material. Figure 4.4 depicts the FTIR spectra of a bare NZSP sample produced at 1050 degrees Celsius. The vibration bands of P-O span from 1100 to 1300 cm^{-1}. Thus, the peak at 1235 cm^{-1} may be related to the stretching vibration of P-O. The peaks at 891 cm^{-1} and 727 cm^{-1} are bending vibrations of Zr-O in ZrO_6^{8-}. The bands in range of 1100-900 cm^{-1} correspond to the O-P-O bond, whilst those at 500-600 cm^{-1} correspond to the P-O-P symmetric stretching mode. Thus, peak at 988 cm^{-1} is attributable to the twisting and stretching vibrations of the O-P-O bond in PO_4^{3-}, whereas the peak at 574 cm^{-1} is the P-O-P symmetric stretch mode. The peak at 562 cm^{-1} exhibits stretching modes of the Si-O bond in SiO_4^{4-} [20].
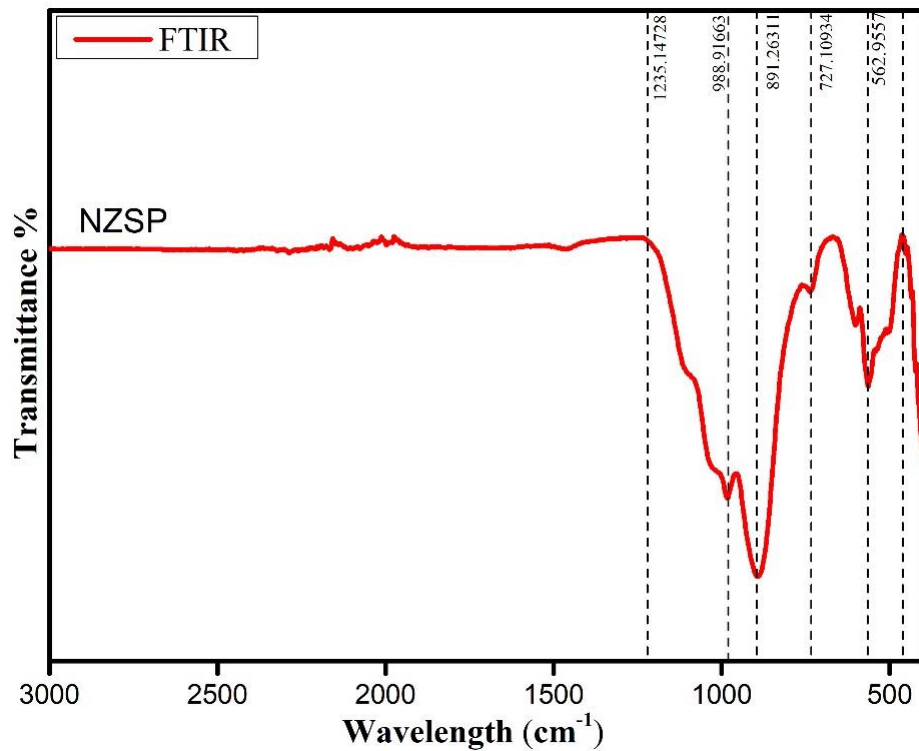
Figure 4.4 FTIR pattern of NZSP calcinated at 1050 °C temperature.

4.4 IMPEDANCE SPECTROSCOPY ANALYSIS

The Nyquist plot of sintered NZSP1050 solid electrolytes at temperatures (30-100 °C) is shown in Figure 4.5. Figure shows two distinct regions, semicircle at high frequency and spike at lower frequency. The high frequency semicircle results from a parallel combination of bulk resistance (R_b) and capacitance, while the lower frequency spike is caused by ion diffusion in the electrolyte. The value of bulk resistance (R_b) may be calculated using the semicircle's x-axis intercept. The semicircle intercepts on the real axis shift towards origin as temperature increases for each composition. As a result, the bulk resistance reduces with increasing temperature. The number of charge carriers rises with increasing temperature.[29]

The real impedance (Z') decreases with increasing frequency and temperature. As temperature increases, the amplitude of Z' drops at lower frequencies before merging at higher frequencies. This is related to the discharge of space charge. As temperature rises, the electrolyte's barrier potential decreases, leading to an increase in ionic conductivity. At higher frequencies, interfacial polarization is removed, causing the Z'

23

spectra to merge completely. The shifting of the Z' plateau suggests the presence of frequency relaxation in the material. Figure 4.5 (inset) illustrates how the imaginary component of impedance Z'' varies with frequency and temperature. The magnitude of Z'' is the maximum at a specific frequency, with a peak-like curve across temperatures. The spreading of peaks with increasing temperature indicates a dispersion of relaxation time. As temperature rises, ions in the polymer electrolyte develop extra conducting routes, resulting in a drop in peak position [30].

The bulk resistance R_b from the complex impedance plot is used to calculate the ionic conductivity of sintered NZSP1050 solid electrolytes. Ionic conductivity is computed using the Equation (4.2).

$$\sigma = \frac{L}{A \times R_b} \qquad (4.2)$$

Where L is the thickness of the pellet, R_b is the bulk resistance of the pellet, and A is the surface area of the pellet. At ambient temperature, the NZSP1050 pellet gives ionic conductivity of 3.26×10^{-4} S/cm.
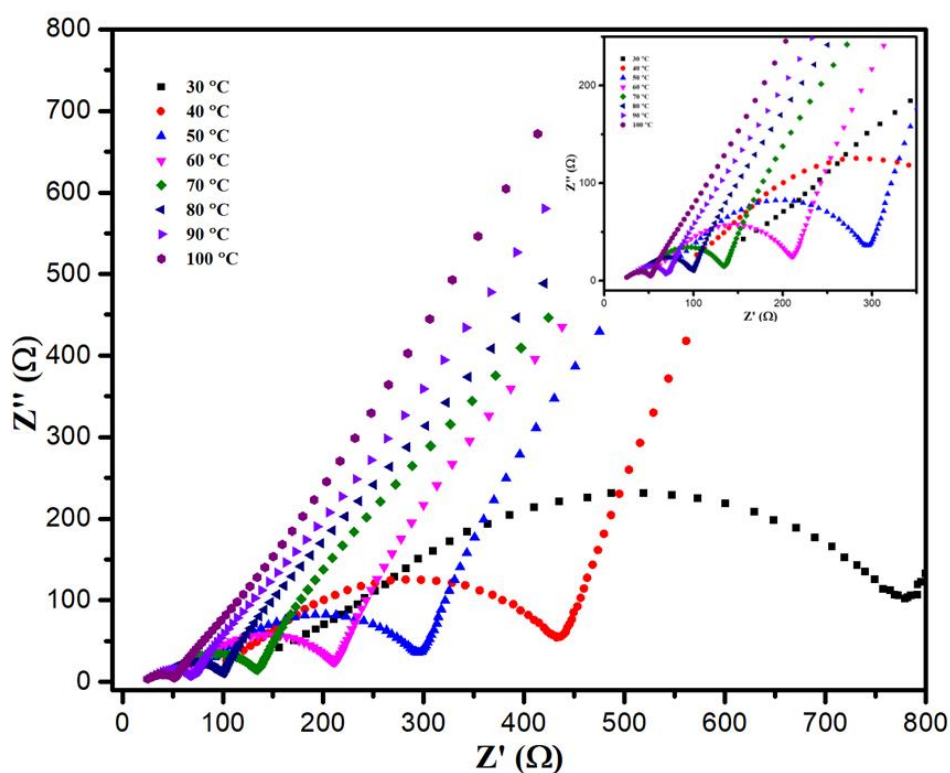

Figure 4.5 Nyquist plot of sintered NZSP1050 pellet.

Figure 4.6 shows the derived Nyquist plot for the NZSP-PEO film. The Nyquist plot shows a semicircle-like curve in the high and medium frequency areas, as well as a spike in the low frequency zone. These findings can be attributed to total resistance, which includes both grain resistance and grain boundary resistance [31]. The grain resistance (R_g) is determined by where the semicircle crosses the real axis at a high frequency. At medium frequency, the spacing between this point and the junction corresponds to the grain-boundary resistance (R_{gb}). Ideally, the grain and grain boundary indicate individual semi-circles but here a single semicircle curve may be due to bulk resistance [32, 33]. As a consequence, the point of intersection at medium frequency reflects the bulk resistance (R_b), including R_g and R_{gb}. To determine electrical conductivity, use the equation (4.2). At ambient temperature, the NZSP-PEO film has the ionic conductivity 1.9×10^{-4} S/cm.
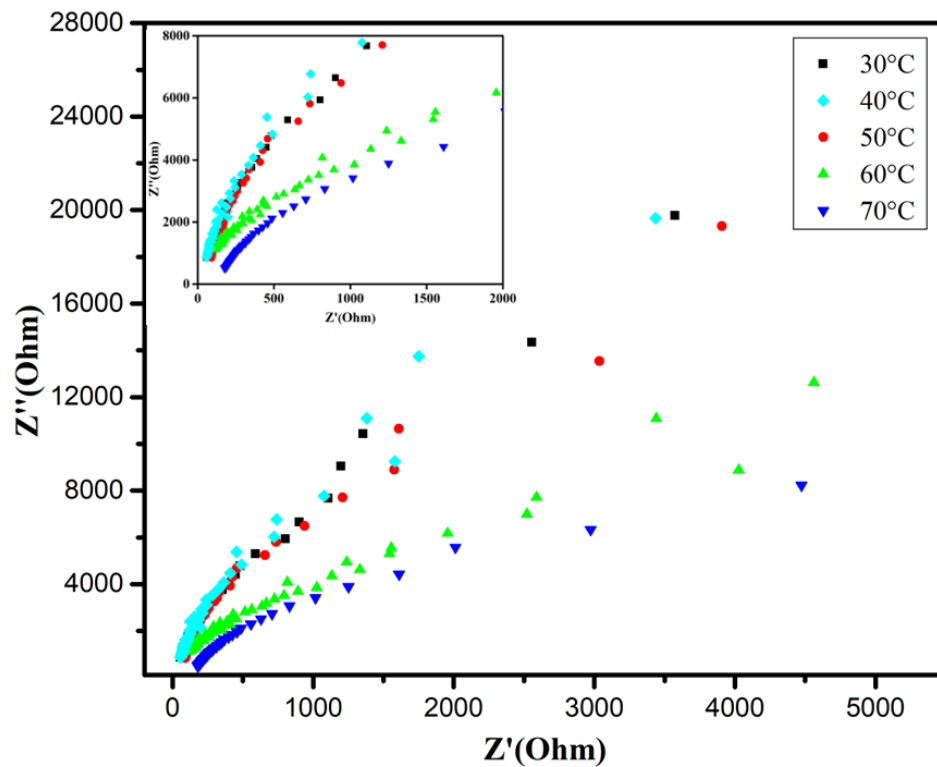

Figure 4.6 Nyquist plot of sintered NZSP1050-PEO film**.**

Measurements of dielectric value provide vital evidence on relaxation mechanism inside the sample, taking into account its temperature and frequency dependence. These tests enable the identification of two critical physical characteristics of a material: electric permittivity (also known as dielectric constant) and dielectric loss. When an alternating field is applied to a sample, charge carriers create heat due to polarization lag, also known as dielectric loss. The loss of electrical energy within a material is caused by both the passage of electric current and dielectric relaxation. Temperature, frequency, orientation, pressure, and molecular structure all impact the material's permittivity, or capacity to store electrical energy[34].

Figure 4.7 (a) NZSP1050 pellet and 4.7 (b) NZSP1050-PEO depicts the temperature dependence of the dielectric constant at certain frequencies. As the frequency rises, the relaxation-type behaviour changes to higher temperatures. Dielectric relaxation in materials is caused by defects like space charge electrons and vacancies. Increased polarization is due to thermally induced activation of carriers, which causes the dielectric constant to rise with temperature. The mechanism of space charge polarization can account for the large increase in dielectric constant at lower frequencies. According to this concept, charge carriers have an increased polarization response at lower frequencies because they closely follow the applied field. This leads in increased permittivity levels. In contrast, at higher frequencies, carriers are unable to properly trace applied field due to the significantly shorter time period. In other words, the applied field changes direction before the carriers can align with it. As a result, net polarization decreases, lowering the dielectric constant. The total dielectric constant is the product of the sample temperature and the frequency of the applied field [35]. In figure 4.7 (b) of NZSP1050-PEO we observe that as the temperature increases above 60 °C there is significantly increase in dielectric constant because PEO starts melting which leads to thermally induced activation of charge carriers.
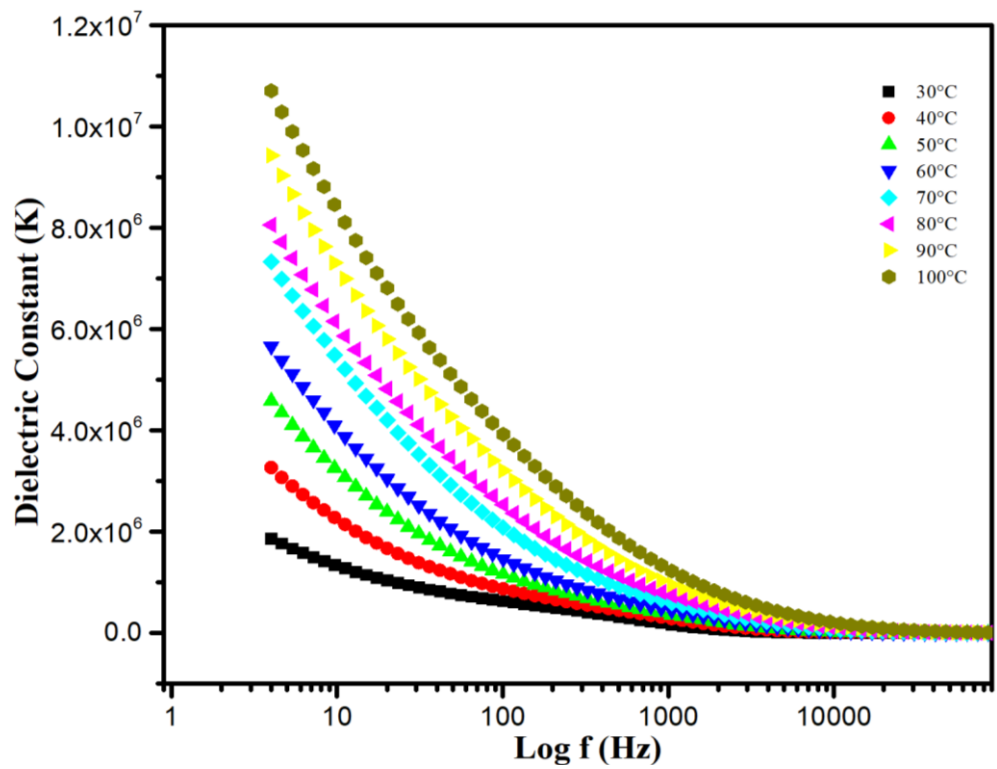
Figure 4.7 (a) Dielectric constant versus log(freq.) of NZSP1050 pellet at various temperatures.
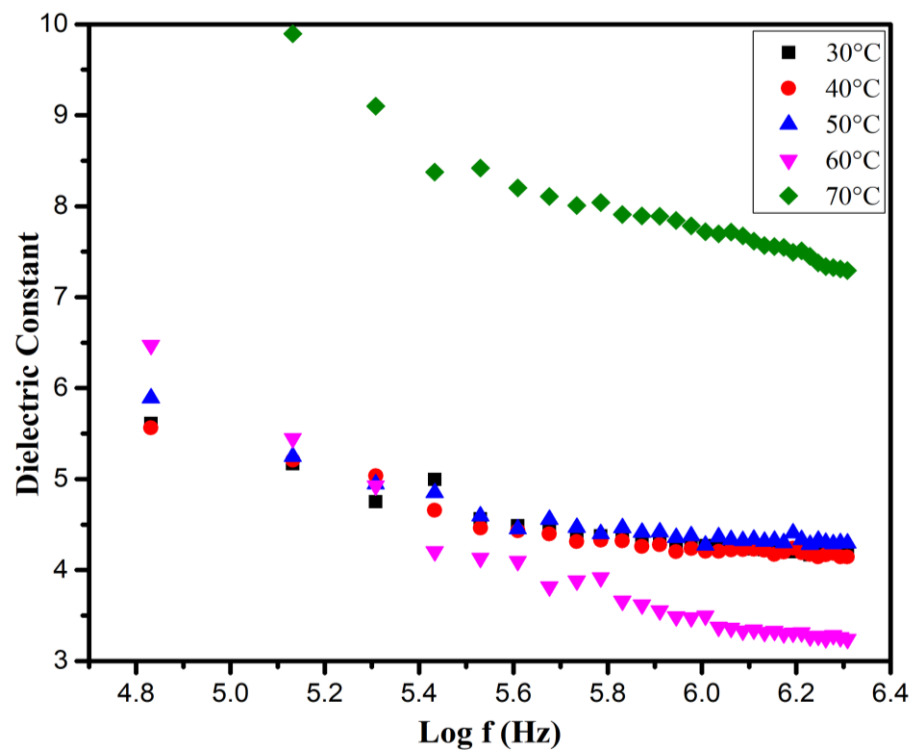

Figure 4.7 (b) Dielectric constant versus log(freq.) of NZSP1050-PEO at various temperatures.

Figure 4.8 (a) NZSP1050 pellet and 4.8 (b) NZSP1050-PEO depicts the temperature-dependent fluctuation of dielectric loss at different frequencies. Dielectric loss is primarily determined by temperature and charge carrier mobility. In figure 4.8 (a) as temperature increases, mobility of charge carriers increases, leading to greater dielectric losses. The loss peak in dielectric loss data occurs once frequency of the applied field matches hopping frequency of the charge carriers. As temperature rises, the loss peak changes to a higher frequency, indicating an increase in charge carrier hopping frequency [36]. In figure 4.8 (b) of NZSP1050-PEO we observe dielectric loss increases significantly it may due to melting of PEO polymer which leads to increase in mobility of charge carriers. Dielectric loss peaks are not observed clearly it may because of less amount of NZSP1050 incorporated in PEO polymer.
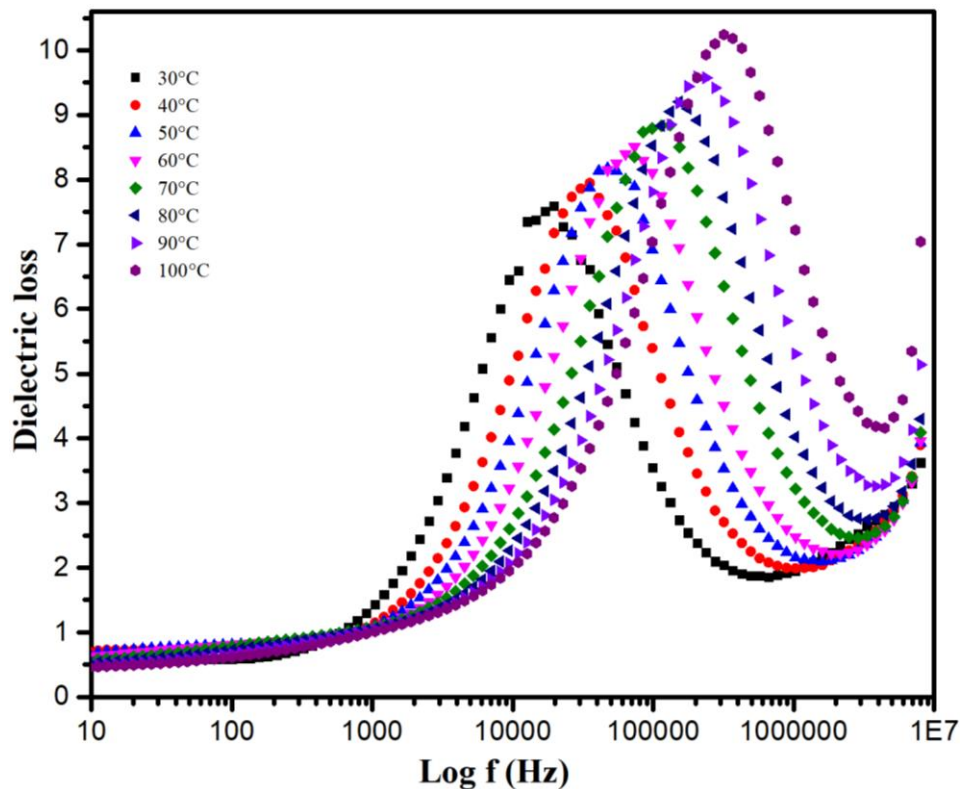

Figure 4.8 (a) Dielectric loss versus log(freq.) of NZSP1050 pellet at various temperatures.
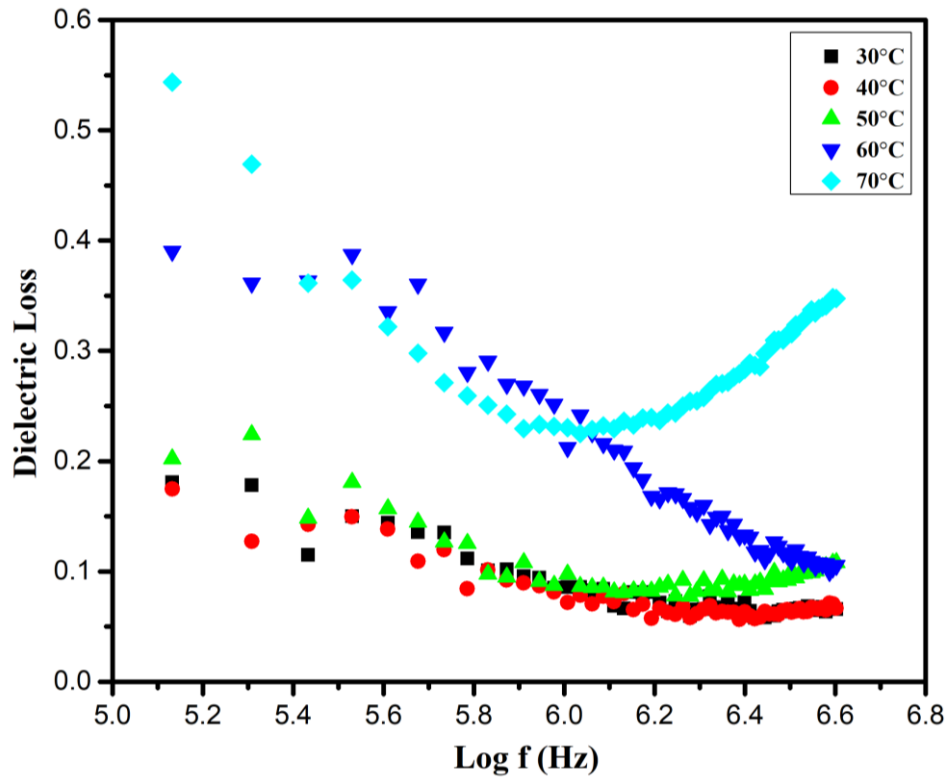
Figure 4.8 (b) Dielectric constant versus log(freq.) of NZSP1050-PEO at various temperatures.

Figure 4.9 depicts the temperature-dependent resistivity curve of the produced NZSP1050-PEO hybrid film between 30 °C and 70 °C. The resistivity behaviour indicates the sample's substantial insulating characteristics at low temperatures. Thermally induced charge carriers travel more readily at higher temperatures, resulting in lower resistance. The Resistivity-Temperature curve exhibits semiconductor-like behaviour. We use the Arrhenius equation of thermal activation to compute the activation energy of thermally produced charge carriers. Figure 4.10 shows the Arrhenius curve for the manufactured material's total conductivity across the observed temperature range of 30 °C - 70 °C. According to the equation, the resistivity data is best fitted using the Equation (4.3).

$$\rho = \rho_0 \exp\left(\frac{E_a}{K_b T}\right) \tag{4.3}$$

Here, T is the temperature, ρ_0 is the preexponential factor, k_B is the Boltzmann constant, E_a is activation energy of charge carriers through thermal conduction, , and ρ is the sample resistivity measured at a certain temperature. The activation energy (E_a) was calculated by analyzing the slope of a linear regression analysis performed on the Arrhenius chart. The NZSP-PEO hybrid film has an E_a of 0.11 eV.
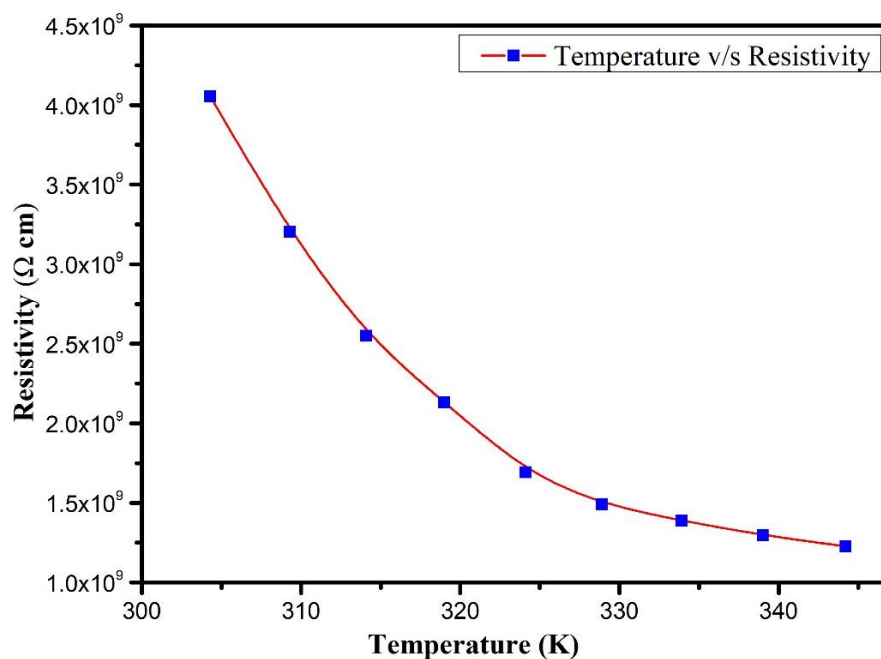

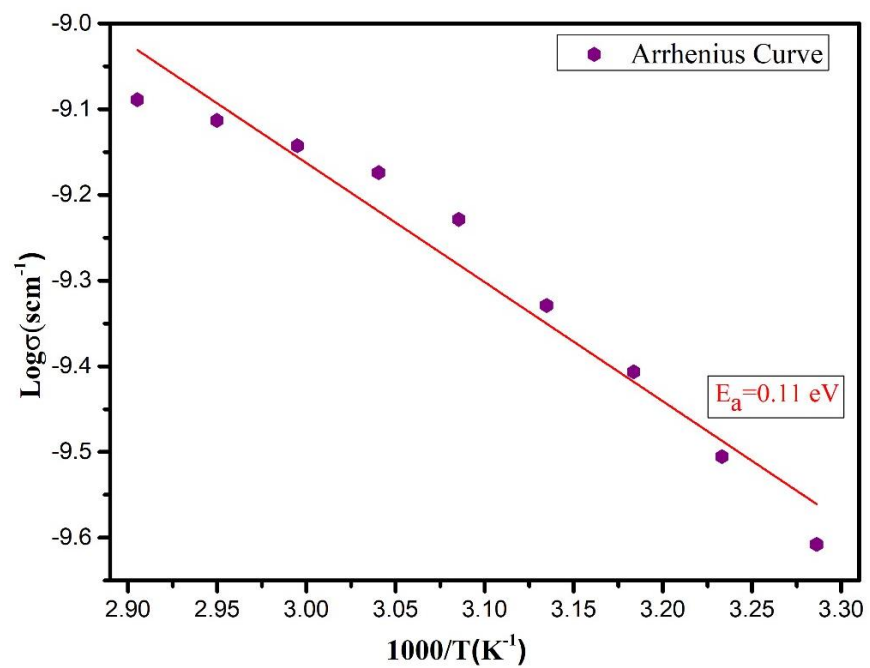**Figure 4.9** Variation of Resistivity with Temperature of NZSP1050-PEO film.

Figure 4.10 Arrhenius plot: variation of conductivity with temperature of NZSP1050-PEO film.

5

SUMMARY AND CONCLUSIONS

$Na_3Zr_2Si_2PO_{12}$ has been successfully synthesized through solid-state route calcinated at different temperatures. XRD confirm the proper phase formation and monoclinic structure (with space group c2/c) of NZSP calcinated at 1050 ˚C. Williamson-Hall plot has been used to estimate the average crystallite size of 133 nm and microstrain of 2.43 x 10^{-3}. SEM images of bare NZSP1050 shows agglomeration and nonuniform spherical particles with average particle sizes ranging from 0.32 μm to 0.52 μm. NZSP1050 pellet has been calcinated at 1150 ˚C and aluminium is uniformly coated on both sides of pellet using thermal vapour deposition technique. Sintered pellet of NZSP1050 gives maximum bulk ionic conductivity of 3.26×10^{-4} S/cm at ambient temperature. NZSP1050 has been successfully blended with PEO polymer to form NZSP1050-PEO composite electrolyte. The determination of the activation energy of the prepared material provided a value of 0.11 eV. Through the examination of conductivity via resistivity-temperature analysis, it is evident that the NZSP1050-PEO film exhibits similarities to a semiconducting like material. NZSP1050-PEO composite film indicates the ionic conductivity of 1.9×10^{-4} S/cm at ambient temperature. The dielectric study shows that as the temperature increases charge carriers increases polarization which leads to increase in dielectric constant at lower frequency. At higher frequencies, carriers are unable to trace applied field due to shorter time period which leads to decrease in polarization and the dielectric constant. Dielectric loss has been determined by charge carrier mobility and the hopping frequency of the charge carriers. As frequency of the applied field matches with hopping frequency of the charge carriers leads to increase in dielectric losses.

The methodology used in the current study provides opportunities for further research into alternative techniques for improving the conductivity of NZSP and customizing the architecture to facilitate the development of high-efficiency electrolytes for solid-state sodium-ion batteries.

REFERENCES

1. Shakun JD, Clark PU, He F, et al (2012) Global warming preceded by increasing carbon dioxide concentrations during the last deglaciation. Nature 2012 484:7392 484:49–54. https://doi.org/10.1038/nature10915

2. Xie Z, Zhang X, Zhang Z, et al (2017) Metal–CO_2 Batteries on the Road: CO_2 from Contamination Gas to Energy Source. Advanced Materials 29:1605891. https://doi.org/10.1002/ADMA.201605891

3. Learn About Batteries - Battery University. https://batteryuniversity.com/articles. Accessed 5 Jun 2024

4. (2019) Secondary battery

5. Long Y, Shu Y, Ma X, Ye M (2014) In-situ synthesizing superior high-rate LiFePO4/C nanorods embedded in graphene matrix. Electrochim Acta 117:105–112. https://doi.org/10.1016/J.ELECTACTA.2013.11.106

6. Chawla N, Bharti N, Singh S (2019) Recent Advances in Non-Flammable Electrolytes for Safer Lithium-Ion Batteries. Batteries 2019, Vol 5, Page 19 5:19. https://doi.org/10.3390/BATTERIES5010019

7. Chawla N, Bharti N, Singh S (2019) Recent advances in non-flammable electrolytes for safer lithium-ion batteries. Batteries 5:. https://doi.org/10.3390/BATTERIES5010019

8. Jie Y, Ren X, Cao R, et al (2020) Advanced Liquid Electrolytes for Rechargeable Li Metal Batteries. Adv Funct Mater 30:1910777. https://doi.org/10.1002/ADFM.201910777

9. Zhang B, Tan R, Yang L, et al (2018) Mechanisms and properties of ion-transport in inorganic solid electrolytes. Energy Storage Mater 10:139–159. https://doi.org/10.1016/J.ENSM.2017.08.015

10. Zhang Z, Zhang Q, Ren C, et al (2016) A ceramic/polymer composite solid electrolyte for sodium batteries. J Mater Chem A Mater 4:15823–15828. https://doi.org/10.1039/C6TA07590H

11. Wang Y, Song S, Xu C, et al (2019) Development of solid-state electrolytes for sodium-ion battery–A short review. Nano Materials Science 1:91–100. https://doi.org/10.1016/J.NANOMS.2019.02.007

12. Shi K, Guan B, Zhuang Z, et al (2024) Recent Progress and Prospects on Sodium-Ion Battery and All-Solid-State Sodium Battery: A Promising Choice of Future Batteries for Energy Storage. Energy and Fuels. https://doi.org/10.1021/ACS.ENERGYFUELS.4C00980/ASSET/IMAGES/MEDIUM/EF4C00980_0058.GIF

13. Boaretto N, Garbayo I, Valiyaveettil-SobhanRaj S, et al (2021) Lithium solid-state batteries: State-of-the-art and challenges for materials, interfaces and processing. J Power Sources 502:229919. https://doi.org/10.1016/J.JPOWSOUR.2021.229919

14. Zhang L, Liu Y, You Y, et al (2023) NASICONs-type solid-state electrolytes: The history, physicochemical properties, and challenges. Interdisciplinary Materials 2:91–110. https://doi.org/10.1002/IDM2.12046

15. Singh K, Chakraborty A, Thirupathi R, Omar S (2022) Recent advances in NASICON-type oxide electrolytes for solid-state sodium-ion rechargeable batteries. Ionics 2022 28:12 28:5289–5319. https://doi.org/10.1007/S11581-022-04765-3

16. Sampathkumar R, Echeverría M, Zhang Y, et al (2023) Interface Stability between Na3Zr2Si2PO12 Solid Electrolyte and Sodium Metal Anode for Quasi-Solid-State Sodium Battery. Batteries 9:8. https://doi.org/10.3390/BATTERIES9010008/S1

17. Fu Y, Liu D, Sun Y, et al (2023) Epoxy Resin-Reinforced F-Assisted Na3Zr2Si2PO12 Solid Electrolyte for Solid-State Sodium Metal Batteries. Batteries 9:331. https://doi.org/10.3390/BATTERIES9060331/S1

18. He S, Xu Y, Chen Y, Ma X (2020) Enhanced ionic conductivity of an F−-assisted Na3Zr2Si2PO12 solid electrolyte for solid-state sodium batteries. J Mater Chem A Mater 8:12594–12602. https://doi.org/10.1039/C9TA12213C

19. Cho SJ, Uddin MJ, Alaboina P (2017) Review of Nanotechnology for Cathode Materials in Batteries. Emerging Nanotechnologies in Rechargeable Energy

Storage Systems 83–129. https://doi.org/10.1016/B978-0-323-42977-1.00003-0

20. Adetona AJ, Wang G, Walkley B, et al (2024) Effect of ZrO2 stoichiometry on the structural and electrical properties of Na3Zr2−xSi2PO12-2x solid electrolyte. J Eur Ceram Soc 44:2989–2997. https://doi.org/10.1016/J.JEURCERAMSOC.2023.12.071

21. Epp J (2016) X-ray diffraction (XRD) techniques for materials characterization. Materials Characterization Using Nondestructive Evaluation (NDE) Methods 81–124. https://doi.org/10.1016/B978-0-08-100040-3.00004-3

22. ELLIOTT PT, GLASS JE (2000) WATER-BORN COATINGS. Applied Polymer Science: 21st Century 563–588. https://doi.org/10.1016/B978-008043417-9/50032-5

23. de Assumpcão Pereira-da-Silva M, Ferri FA (2017) Scanning Electron Microscopy. Nanocharacterization Techniques 1–35. https://doi.org/10.1016/B978-0-323-49778-7.00001-1

24. Petit S, Madejova J (2013) Fourier Transform Infrared Spectroscopy. Dev Clay Sci 5:213–231. https://doi.org/10.1016/B978-0-08-098259-5.00009-3

25. Macdonald JR, Johnson WB (2018) Fundamentals of Impedance Spectroscopy. Impedance Spectroscopy 1–20. https://doi.org/10.1002/9781119381860.CH1

26. Impedance Spectroscopy - Chemistry LibreTexts. https://chem.libretexts.org/Courses/Franklin_and_Marshall_College/Introduction_to_Materials_Characterization__CHM_412_Collaborative_Text/Electrochemistry/Impedance_Spectroscopy. Accessed 5 Jun 2024

27. Gordon RS, Miller GR, McEntire BJ, et al (1980) Fabrication and characterization of NASICON electrolytes

28. Fuentes RO, Figueiredo FM, Marques FMB, Franco JI (2001) Processing and electrical properties of NASICON prepared from yttria-doped zirconia precursors. J Eur Ceram Soc 21:737–743. https://doi.org/10.1016/S0955-2219(00)00264-8

29. Verma ML, Sahu HD (2017) Study on ionic conductivity and dielectric properties of PEO-based solid nanocomposite polymer electrolytes. Ionics

(Kiel) 23:2339–2350. https://doi.org/10.1007/S11581-017-2063-4/FIGURES/15

30. Jadaun SS, Panwar AK, Geetanjali (2024) The Effect of Multi-step Sintering on the density of Li7La3Zr1.75Ce0.25O12 as Solid State Electrolyte Material. Indian Journal of Pure & Applied Physics (IJPAP) 62:116–123. https://doi.org/10.56042/IJPAP.V62I2.7700

31. Xu B, Duan H, Xia W, et al (2016) Multistep sintering to synthesize fast lithium garnets. J Power Sources 302:291–297. https://doi.org/10.1016/J.JPOWSOUR.2015.10.084

32. Kiran Kumar K, Ravi M, Pavani Y, et al (2011) Investigations on the effect of complexation of NaF salt with polymer blend (PEO/PVP) electrolytes on ionic conductivity and optical energy band gaps. Physica B Condens Matter 406:1706–1712. https://doi.org/10.1016/J.PHYSB.2011.02.010

33. Wu M, Liu D, Qu D, et al (2020) 3D Coral-like LLZO/PVDF Composite Electrolytes with Enhanced Ionic Conductivity and Mechanical Flexibility for Solid-State Lithium Batteries. ACS Appl Mater Interfaces 12:52652–52659. https://doi.org/10.1021/ACSAMI.0C15004/ASSET/IMAGES/LARGE/AM0C15004_0005.JPEG

34. Meena R, Dhaka RS (2022) Dielectric properties and impedance spectroscopy of NASICON type Na3Zr2Si2PO12. Ceram Int 48:35150–35159. https://doi.org/10.1016/J.CERAMINT.2022.08.111

35. Sumi S, Rao PP, Deepa M, Koshy P (2010) Electrical conductivity and impedance spectroscopy studies of cerium based aeschynite type semiconducting oxides: CeTiMO6 (M=Nb or Ta). J Appl Phys 108:. https://doi.org/10.1063/1.3481389/348500

36. Anju Balaraman A, Dutta S (2022) Inorganic dielectric materials for energy storage applications: a review. J Phys D Appl Phys 55:183002. https://doi.org/10.1088/1361-6463/AC46ED

PLAGRISM REPORT

PAPER NAME

Thesis Puneet kumar (2k22/MSCPHY/32
)_Sourav meena (2k22/MSCPHY/41)

AUTHOR

Puneet kumar and Sourav meena

WORD COUNT

7567 Words

CHARACTER COUNT

45290 Characters

PAGE COUNT

46 Pages

FILE SIZE

3.4MB

SUBMISSION DATE

Jun 8, 2024 1:43 PM GMT+5:30

REPORT DATE

Jun 8, 2024 1:44 PM GMT+5:30

● 7% Overall Similarity

The combined total of all matches, including overlapping sources, for each database.

- 5% Internet database
- Crossref database
- 3% Submitted Works database

- 4% Publications database
- Crossref Posted Content database

● Excluded from Similarity Report

- Bibliographic material
- Cited material

- Quoted material
- Small Matches (Less then 10 words)

37

● **7% Overall Similarity**

Top sources found in the following databases:

- 5% Internet database
- Crossref database
- 3% Submitted Works database
- 4% Publications database
- Crossref Posted Content database

TOP SOURCES

The sources with the highest number of matches within the submission. Overlapping sources will not be displayed.

1	**link.springer.com** Internet	**2%**
2	**Mohan L. Verma, Homendra D. Sahu. "Study on ionic conductivity and ...** Crossref	**<1%**
3	**University of Petroleum and Energy Studies on 2024-06-08** Submitted works	**<1%**
4	**Lixiao Zhang, Yimeng Liu, Ya You, Ajayan Vinu, Liqiang Mai. "NASICON...** Crossref	**<1%**
5	**coursehero.com** Internet	**<1%**
6	**K. Naveen Kumar, L. Vijayalakshmi, Jong Su Kim, Jaesool Shim, Migyu...** Crossref	**<1%**
7	**unbscholar.lib.unb.ca** Internet	**<1%**
8	**Ramcharan Meena, Rajendra S. Dhaka. "Dielectric properties and impe...** Crossref	**<1%**

Sources overview

38

21 Kim, T.J.. "Ionic conductivity of Li"xB"1"-"x"/"3PO"4 ceramic electrolyte ...   <1%
    Crossref

22 Wei Liu, Qiao Wang, Quan Ouyang, Xin Zhang, Yaowen Wang, Haitong ...   <1%
    Crossref

23 arxiv.org   <1%
    Internet

24 iopscience.iop.org   <1%
    Internet

25 pubs.rsc.org   <1%
    Internet

26 shodh.inflibnet.ac.in:8080   <1%
    Internet

27 researchgate.net   <1%
    Internet

CONFERENCE RECORD

PROOF OF REGISTRATION

**International Conference on Atomic, Molecular, Material,
Nano and Optical Physics with Applications
(ICAMNOP–2023)**
Organized by: Department of Applied Physics,
Delhi Technological University Delhi-110042, India
December 20th-22nd, 2023
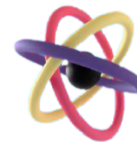
PAYMENT RECEIPT

BILL TO
Mr. SOURAV MEENA
7976893337
souravkamlesh.meena@gmail.com

RECEIPT NO.
276/231205133232
AMOUNT
4885.20INR
DATETIME
05-12-2023 13:39:42

PAYMEN DETAILS	
Transaction Id	: 276/231205133232
Payment Method	: Credit/Debit Card
Payment Gatway	: Stripe Payment Gatway

Note:
This is a computer generated receipt and no signature is required.

PARTICIPATION CERTIFICATES

CARBOXXXVII

**International Conference on Basic, Analytical and Allied Sciences
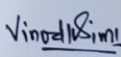at the Interface of Carbohydrates and Biomass Valorisation**

30th November – 2nd December 2023

Certificate of Participation

This is to certify that Prof. / Dr. / Mr. / Ms. PUNEET KUMAR

of DELHI TECHNOLOGICAL UNIVERSITY

has attended this conference organized by Department of Applied Chemistry, Delhi Technological University, Delhi – 110042, India in association with Association of Carbohydrate Chemists and Technologists (India) & Indian Society of Analytical Scientists-Delhi Chapter at Delhi Technological University. He / She has participated as Invited Speaker / Session Chair / Organizer / Oral Paper Presenter / Poster Paper Presenter / Delegate / Sponsor in this CARBOXXXVII.

Prof. Anil Kumar
Chairman

Prof. Ram Singh
Convener cum Organizing
Secretary

Prof. Vinod K. Tiwari
Hony. Secretary ACCTI

PROOF OF ACCEPTANCE

Dear Dr Amrish Panwar,

We are pleased to inform you that your paper

045: "Impact of Calcination Temperature on Structural Properties of Na3Zr2Si2PO12 as a Solid Electrolyte for Na-ion Batteries"
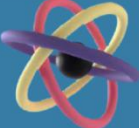
has been accepted for

International Conference on Atomic, Molecular, Material, Nano, and Optical Physics with Applications (ICAMNOP-2023)

SCOPUS INDEXING

International Conference on Atomic, Molecular, Material, Nano and Optical Physics with Applications (ICAMNOP–2023)

Organized by: Department of Applied Physics, Delhi Technological University Delhi-110042, India

December 20th-22nd, 2023

HOME   CONFERENCE COMMITTEE SPEAKERS PUBLICATION REGISTRATION ABSTRACTS ACCOMMODATION TOUR GALLERY CONTACT US

Login

Publication

The papers will be published in the Scopus indexed Springer's Proceedings in Physics (https://www.springer.com/series/361) after peer review.

Proceedings of our last International conference CAMNP 2019 was also published in Scopus indexed Springer's Proceedings in Physics
https://link.springer.com/book/10.1007/978-981-16-7691-8